Greenhouse Warming Reduces Global Energy Conversion into Oceanic Lee Waves

Zhibin Yang[1], Zhao Jing[1, 2], and Xiaoming Zhai[3]

[1]Frontier Science Center for Deep Ocean Multispheres and Earth System (FDOMES) and Physical Oceanography Laboratory, Ocean University of China, Qingdao, China.

[2]Laoshan Laboratory, Qingdao, China.

[3]Centre for Ocean and Atmospheric Sciences, School of Environmental Sciences, University of East Anglia, Norwich, United Kingdom.

Corresponding author: Zhao Jing (jingzhao198763@sina.com)

Key Points:

- The response of energy conversion into lee waves to greenhouse warming is investigated with a high-resolution coupled global climate model.
- Lee wave conversion rate is projected to decrease by ~20% by the end of 21st century under the high carbon emission scenario.
- This decrease is attributed to the weakened bottom large-scale flows, mesoscale eddies and stratification.

Abstract

Oceanic lee waves play an important role in dissipating wind-driven ocean circulations and powering turbulent diapycnal mixing. Here we investigate impacts of the greenhouse warming on global energy conversion into lee waves using a linear theory of lee wave generation and output from a high-resolution (0.1° for the ocean) coupled global climate model. The global energy conversion rate into lee waves under the historical (1930s) climate condition is estimated to be 193.0±3.0 GW. Under the high carbon emission scenario, this conversion rate is projected to decrease by about 20% by the end of 21st century, due to weakened bottom large-scale mean flows, mesoscale eddies and stratification. The decrease of the conversion rate is widespread and particularly pronounced in the Gulf Stream and Drake Passage. Our results suggest significant response of oceanic lee waves to the greenhouse warming, with implications for future changes of global ocean circulations and climate.

Plain Language Summary

Oceanic lee waves, a kind of stationary internal gravity waves, are generated when bottom flows impinge on small-scale uneven topography. They provide an energy pathway from wind-driven large-scale circulations to microscale turbulent mixing. Theories predict that the energy conversion into lee waves depends on the stratification and flow speed near the sea floor, both of which are likely to weaken under the greenhouse warming. In this study, we use a high-resolution coupled global climate model to estimate the response of global energy conversion into lee waves to the greenhouse warming. Our results show that, under the high carbon emission scenario, the global energy conversion into lee waves at the end of the 21st century will decrease by 20% compared to its level in the 1930s. This decrease in the energy conversion has important implications for future changes of global ocean circulations and climate.

1 Introduction

Oceanic lee waves are generated via the interactions of bottom geostrophic flows with small-scale topography characterized by wavelengths typically ranging from 0.1 to 10.0 km (Bell, 1975a, b). These waves can extract energy from the geostrophic flows and radiate upward into the ocean interior. When lee waves break due to the wave-wave interactions or shear instability, the energy extracted from the geostrophic flows is dissipated and a fraction of it is converted into ocean turbulent diapycnal mixing (e.g., Nikurashin et al., 2013).

The global energy conversion rate from geostrophic flows into lee waves is estimated to range from 0.2 to 0.75 TW, depending on the datasets and methods for estimation (Nikurashin & Ferrari, 2011; Scott et al., 2011; Wright et al., 2014). Despite the large difference of overall magnitude of the energy conversion rate, its geographical distribution is consistent across these studies, with the Southern Ocean (SO) playing a dominant role. In view that the global wind work into the surface geostrophic currents is estimated to be around 1 TW (Wunsch, 1999), the generation of lee waves could be an important energy sink for wind-driven ocean circulations and a source for deep-ocean turbulent diapycnal mixing (Munk & Wunsch, 1998; Wunsch & Ferrari, 2004). Several studies based on observations (Brearley et al., 2013; Clément et al., 2016; Cusack et al., 2017; Evans et al., 2020; Hu et al., 2020; Meyer et al., 2016) and numerical models

(Trossman et al., 2013; Trossman et al., 2016; Melet et al., 2014; Nikurashin et al., 2013; Yang et al., 2021; Yang et al., 2022; Yang et al., 2023b) have highlighted the important role of lee waves in regulating the ocean energetics, powering turbulent diapycnal mixing, which in turn impacts the global climate system. Understanding the response of lee wave generation to the greenhouse warming is thus important for accurately predicting future climate changes.

Melet et al. (2015) investigated the changes of global energy conversion rate into lee waves under different warming scenarios using the linear theory (Bell, 1975a, b) and a coarse-resolution coupled global climate model (CGCM). They reported that the global energy conversion rate into lee waves is projected to decrease by about 20% by the end of the 22nd century under a high carbon emission scenario mainly due to the weakening of the model-resolved large-scale mean flows near the sea floor. However, the oceanic resolution of their CGCM, i.e., 1^{o}, is insufficient to resolve the ocean mesoscale eddies that make dominant contribution to the total kinetic energy of the geostrophic flows (Ferrari & Wunsch, 2009). The parameterization they used to estimate the unresolved mesoscale eddy velocity relies on some arbitrary parameter choices in the mesoscale energy closure (Eden & Greatbatch, 2008; Marshall & Adcroft, 2010), which causes uncertainties in their estimated global energy conversion rate into lee waves and its future change.

In this study, we evaluate the response of the global energy conversion into lee waves to the greenhouse warming using an eddy-resolving (0.1° for the ocean) Community Earth System Model (hereinafter CESM-HR for short; Chang et al., 2020). The paper is organized as follows. Section 2 describes the linear theory of lee wave generation and the configurations of the CESM-HR. In Section 3, we compare the energy conversion rates into lee waves in the historical period (1930-1934) and in the end of the 21st century under the high carbon emission scenario, and analyze the factors responsible for the changes of the energy conversion rate. Effects of the Froud number are discussed in Section 4 followed by a summary in Section 5.

2 Methodology

2.1. Linear theory of lee wave generation

In the case of sub-critical topography where slope of ocean topography is smaller than slope of radiating lee waves, the energy conversion rate from geostrophic flows into lee waves E can be derived from the linear theory (Bell, 1975a, b):

$$E = \frac{\rho_0}{4\pi^2}\int_{-\infty}^{+\infty}\int_{-\infty}^{+\infty} P(k,l)\frac{(\mathbf{U}_b\cdot\mathbf{k})}{|\mathbf{k}|}\sqrt{N_b^2-(\mathbf{U}_b\cdot\mathbf{k})^2}\cdot\sqrt{(\mathbf{U}_b\cdot\mathbf{k})^2-f^2}\,dkdl\,, \qquad (1)$$

where ρ_0 is the reference density, $\mathbf{k}=(k,l)$ is the horizontal wavenumber, $P(k,l)$ is the two-dimensional topographic spectrum, N_b and $\mathbf{U}_b$ are the bottom stratification (buoyancy frequency) and bottom velocity, and f is the Coriolis frequency.

Eq. (1) is applicable only to the sub-critical topography. To account for the saturation of E over the super-critical topography (Nikurashin & Ferrari, 2010), the value of E in Eq. (1) is multiplied by a factor of $(Fr_c/Fr)^2$ for $Fr > Fr_c$, where $Fr = N_b h/U_b$ is the Froude number with h the root-mean-squared height of the small-scale topography and Fr_c is the critical Froude number. In this study, Fr_c is set as 0.5 following Aguilar and Sutherland (2006), but other values of Fr_c (0.4 and 0.75) are also adopted to test the influences of Fr_c on the future change of E.

123 2.2. Topographic spectrum

124 The topographic spectrum model proposed by Goff and Jordan (1988) is used to
125 represent the small-scale topographic features:

126 $$P(k,l)=\frac{2\pi H^2(\mu-2)}{k_0 l_0}\left[1+\frac{k^2}{k_0{}^2}\cos^2(\phi-\phi_0)+\frac{l^2}{l_0{}^2}\sin^2(\phi-\phi_0)\right]^{-\mu/2}, \quad (2)$$

127 where H^2 is the variance of the full topographic height, μ is the roll-off slope at high
128 wavenumber, ϕ_0 is the azimuthal angle and (k_0,l_0) are the characteristic wavenumbers. Goff
129 (2010) (hereinafter G2010 for short) derived the values of these topographic parameters from
130 satellite observations. In this study, we adopt the G2010's estimates that have been widely used
131 in estimating E (e.g., Baker & Mashayek, 2022; Scott et al., 2011; Yang et al., 2018). It should
132 be noted that $P(k,l)$ of G2010 is not available everywhere (Figure. 1). We reminder readers that
133 the "global ocean" in this study actually refers to the region where $P(k,l)$ of G2010 is available.

134 2.3. Eddy-mean flow decomposition

135 The geostrophic flows consist of the large-scale mean flows and mesoscale eddies.
136 Correspondingly, E can be decomposed into contributions by large-scale mean flows (E_{LM}) and
137 mesoscale eddies (E_{ME}) defined as (Yang et al., 2018):

138

139 $$E_{LM}=-\bar{\boldsymbol{\tau}}\cdot\overline{\mathbf{U}_b}, \quad (3)$$

140 $$E_{ME}=-\overline{\boldsymbol{\tau}'\cdot\mathbf{U}_b'}, \quad (4)$$

141 where $\boldsymbol{\tau}=-\frac{\rho_0}{4\pi^2}\int_{-\infty}^{+\infty}\int_{-\infty}^{+\infty}P(k,l)\frac{\mathbf{k}}{|\mathbf{k}|}\sqrt{N_b{}^2-(\mathbf{U}_b\cdot\mathbf{k})^2}\cdot\sqrt{(\mathbf{U}_b\cdot\mathbf{k})^2-f^2}\,dkdl$ is the wave drag vector,
142 the overbar denotes the annual average (large-scale mean flows) and the prime denotes the
143 anomaly (mesoscale eddies).

144 2.4. CESM-HR

145 The CESM-HR is used to simulate the long-term changes of N_b and $\mathbf{U}_b$ under the
146 greenhouse warming. The CESM-HR has a nominal resolution of 0.1° (0.25°) for its oceanic
147 (atmospheric) component. There are 62 vertical levels in the ocean with a maximum grid size of
148 250 m at the 6000-m depth. The simulation is branched off from a 500-year-long pre-industrial
149 control simulation (PI-CTRL) at the 250th model year and integrated to 2100 with a historical run
150 spanning from 1850 to 2005, followed by a future transient climate run from 2006 to 2100 under
151 the representative concentration pathway 8.5 (RCP8.5) scenario. The monthly mean temperature,
152 salinity and three-dimensional velocity are saved during the simulation. In addition, there are
153 daily output for these variables during 1930-1934 (historical period) and 2086-2090 (future
154 period).

155 In this study, N_b is computed as the value of N at the vertical level just over the sea
156 floor, while $\mathbf{U}_b$ is computed as the vertically averaged $\mathbf{U}$ within 0-500 m over the sea floor

(Yang et al., 2018). The model drift after 250 year's spin-up is negligible for $\mathbf{U}_b$ but less so for N_b (Figure S1 in the Supporting Information). This may bias the simulated long-term change of E under the greenhouse warming. To minimize such bias, we subtract the linear trend of N_b during the model years 250-500 in PI-CTRL from N_b during 1850-2100. Then the daily $\mathbf{U}_b$ and the time-mean N_b during 1930-1934 (2086-2090) are substituted into Eq. (1) to estimate E in the historical (future) period. The inter-annual variability of E within each five-year period is found to be much smaller than the difference of E between these two periods (Table 1), lending support that the five-year period is sufficiently long to get statistically robust results.

3 Results

3.1. Energy conversion into lee waves in the historical period simulated by the CESM-HR

The time-mean N_b during the historical period in the CESM-HR is spatially inhomogeneous and generally consistent with that derived from observations (Figure. 1a). Weak bottom stratification with $N_b \sim O(10^{-4}\ \mathrm{s}^{-1})$ is found in most parts of the ocean, whereas large $N_b \sim O(10^{-3}\ \mathrm{s}^{-1})$ is mainly concentrated along shallow mid-ocean ridges. The spatial variability of time-mean $\mathrm{KE}_b = (\mathbf{U}_b \cdot \mathbf{U}_b)/2$ is even more pronounced, varying by three orders of magnitude (Figure. 1b). Large $\mathrm{KE}_b \sim O(10^{-2}\ \mathrm{m}^2/\mathrm{s}^2)$ occurs along the western boundaries of ocean basins, the SO and the eastern tropical Pacific, whereas small $\mathrm{KE}_b \sim O(10^{-5}\ \mathrm{m}^2/\mathrm{s}^2)$ is mainly distributed in the gyre interior.

Consistent with the existing literature (Nikurashin & Ferrari, 2011; Scott et al. 2011), the spatial distribution of time-mean E during the historical period shows large values in the SO, the western boundaries of ocean basins and the eastern tropical Pacific (Figure. 1c). The globally integrated time-mean E during 1930-1934 is 193±3.0 GW (hereinafter the errorbar represents the 95% confidence interval), close to the lower bound of the previous estimates (Nikurashin & Ferrari, 2011).

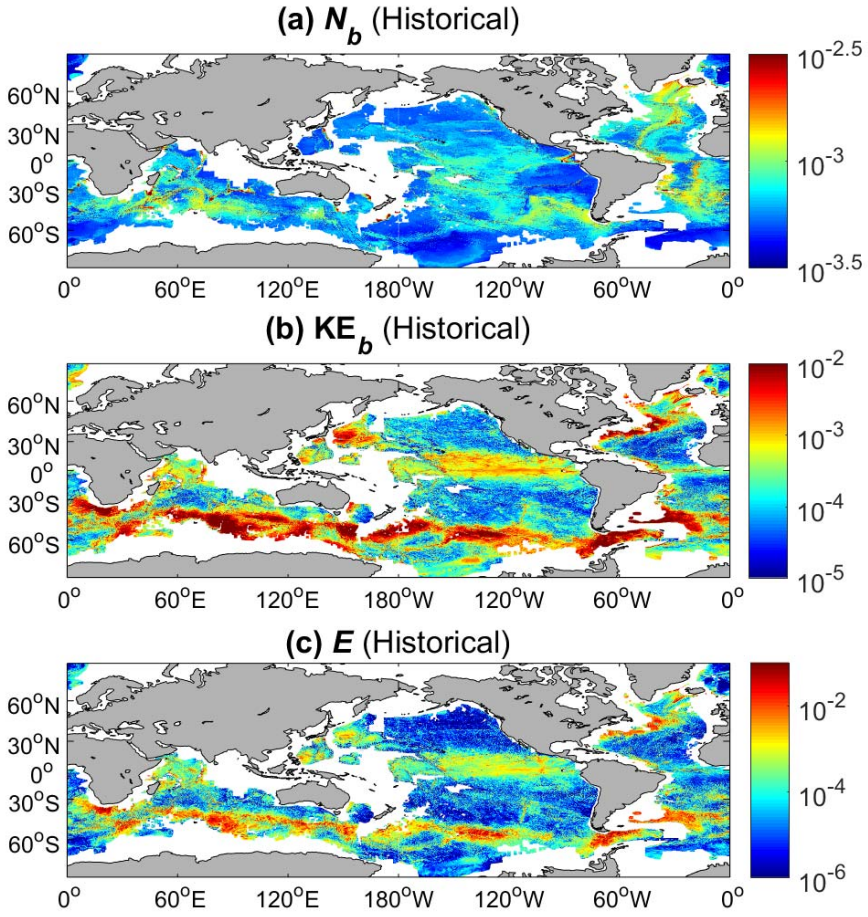

Figure 1. Time-mean (a) bottom stratification N_b (s^{-1}), (b) bottom kinetic energy KE_b (m^2/s^2) and (c) energy conversion rate into lee waves E (W/m^2) during 1930-1934 simulated by the CESM-HR. Regions where the topographic spectrum of G2010 is unavailable are masked by white.

3.2. Response of energy conversion into lee waves to the greenhouse warming

As suggested by Eq. (1), N_b and KE_b are the two important factors determining the magnitude of E. To understand the change of E under the greenhouse warming, the differences of time-mean N_b and KE_b between 1930-1934 and 2086-2090 are examined. Because the geographical distribution of E is highly inhomogeneous (Figure. 1c), we focus on the differences in the regions with $E > 0.52$ mW/m^2 (indicated by color shading in Figure. 2a and b). In particular, these regions only cover a quarter of the ocean area but contribute to ~90% of the total E. These regions are referred to as the active-E ocean hereinafter.

Figure. 2a shows the difference of time-mean N_b between 1930-1934 and 2086-2090 over the active-E ocean. There is a decrease of N_b under the greenhouse warming in most parts

of the active-*E* ocean. Patches of enhanced N_b are mainly confined to the SO (e.g., 60°W-120°E) and the high-latitude regions of the North Atlantic. The time-mean N_b averaged over the active-*E* ocean decreases by 6.5% in response to the greenhouse warming. This appears contrary to the findings of Melet et al. (2015) who reported an overall increase of N_b in a warming climate but is qualitatively consistent with the projections from the high-resolution CGCMs in the Coupled Model Intercomparison Project Phase 6 (CMIP6) archive (Eyring et al., 2016; Table S1 and Figure S2 in the Supporting Information). Furthermore, it should be noted that the calculation made by Melet et al. (2015) covers the entire ocean and includes regions with small *E* values, which can lead to misleading conclusions about the effects of N_b change on *E* change. For example, N_b along the shallow mid-ocean ridges increases significantly under the greenhouse warming (not shown). But the increase of N_b there should contribute little to the change of globally integrated *E*.

The value of KE_b decreases under the greenhouse warming over most parts of the active-*E* ocean, with patches of increased KE_b in the SO. The overall reduction of KE_b under the greenhouse warming could partially result from the enhanced baroclinicity of the ocean caused by the faster warming in the upper than the deeper ocean (Peng et al., 2022). The most notable decrease of KE_b is located in the Gulf Stream, the Drake Passage and the Kerguelen Plateau, where the time-mean KE_b during 2086-2090 is less than 50% of that during 1930-1934. Such regional strong response of KE_b to the greenhouse warming may be related to multiple dynamical processes. For example, it has been well recognized that the slowdown of the Atlantic meridional overturning circulation in a warming climate will weaken the Gulf Stream (e.g., Beech et al., 2022; Chen et al., 2019; Yang et al., 2016).

The globally integrated time-mean *E* during 2086-2090 decreases to 155.5±4.8 GW, a ~20% reduction compared to 193.0±3.0 GW during 1930-1934 (Table 1). The change of *E* under the greenhouse warming is spatially inhomogeneous and generally resembles that of KE_b (Figure. 2b and c). To quantify the respective contribution of the changes of N_b and KE_b to the change of *E*, we recompute *E* during 2086-2090 by either fixing N_b or KE_b as their historical values, denoted as E_{N-fix} and E_{U-fix} respectively (Table 1). The globally integrated time-mean E_{N-fix} (166.9±4.5 GW) and E_{U-fix} (176.5±3.2 GW) during 2086-2090 are close to each other and significantly smaller than the globally integrated time-mean *E* (193.0±3.0 GW) during 1930-1934. Therefore, both the weakened N_b and KE_b contribute importantly to the reduction of *E* under the greenhouse warming. Nevertheless, the relative importance of N_b and KE_b changes in determining the change of *E* is region-dependent (Figure. 2). For instance, the reduced *E* under the greenhouse warming in the Gulf stream and the Drake Passage is primarily explained by the decreased KE_b, whereas the reduced *E* in the Pacific section of SO (e.g., 120°W-150°W) is largely attributed to the reduced N_b there.

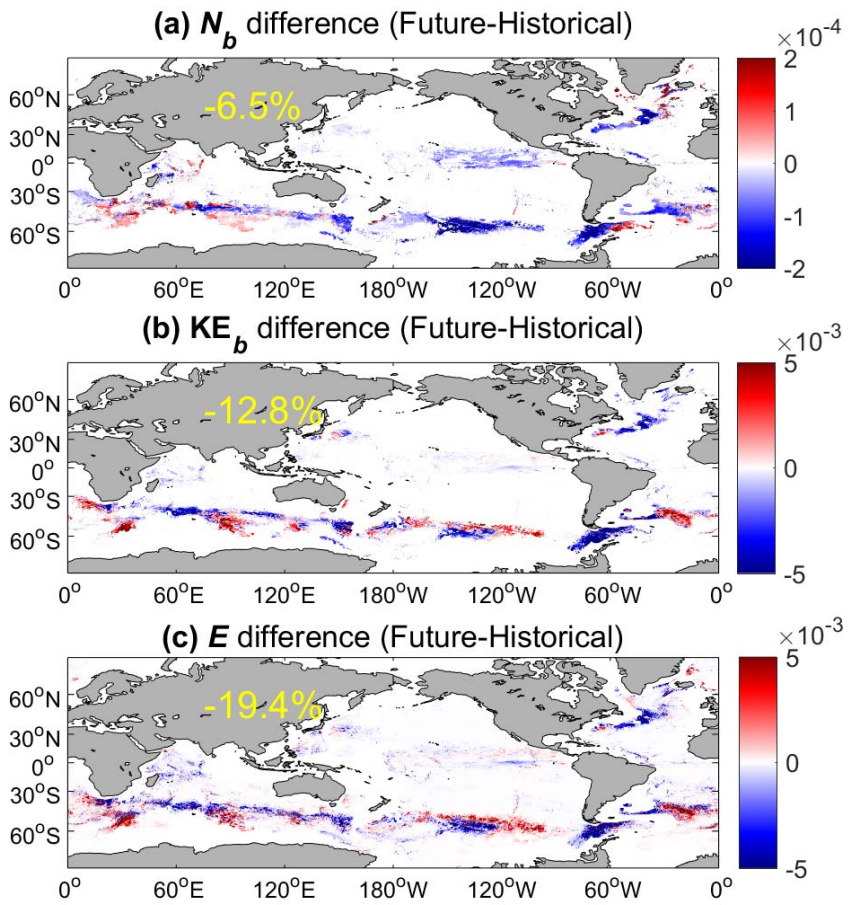

Figure 2. Change of time-mean (a) bottom stratification N_b (s^{-1}), (b) bottom kinetic energy KE_b (m^2/s^2) and (c) energy conversion rate into lee waves E (W/m^2) during 2086-2090 relative to their counterparts during 1930-1934 simulated by the CESM-HR. (a) and (b) only show the results in the active-E ocean. Yellow numbers indicate the percentage changes of N_b and KE_b averaged over the active-E ocean in (a) and (b), but the percentage change of E averaged over the global ocean in (c).

Table 1. The globally integrated time-mean energy conversion rate into lee waves E under different conditions of N_b and $\mathbf{U}_b$ and using different values of Fr_c. The errorbar corresponds to the 95% confidence interval.

N_b (s^{-1})	$\mathbf{U}_b$ (m/s)	Fr_c	E (GW)
Historical	Historical	0.5	193.0±3.0
Historical	Historical	0.4	179.4±2.8
Historical	Historical	0.75	218.3±3.4
Future	Future	0.5	155.5±4.8
Future	Future	0.4	142.4±4.2
Future	Future	0.75	169.3±5.6
Historical	Future	0.5	166.9±4.5
Future	Historical	0.5	176.5±3.2

3.3. Role of mesoscale eddies in the change of energy conversion into lee waves under the greenhouse warming

Both the interactions of large-scale mean flows and mesoscale eddies with topography generate lee waves. The time-mean E_{ME} and E_{LM} during 1930-1934 share similar spatial distributions (Figure. 3a and b). However, E_{ME} is systematically larger in magnitude than E_{LM} and accounts for two-thirds of the globally integrated time-mean E, consistent with the dominant contribution of mesoscale eddies to the total kinetic energy of geostrophic flows (Wunsch & Ferrari, 2004). Under the greenhouse warming, the values of E_{ME} and E_{LM} are reduced over most parts of the global ocean (Figure. 3c and d). The globally integrated time-mean E_{ME} during 2086-2090 is 20.5% smaller than that during 1930-1934, close to the 17.1% reduction for E_{LM}. However, as E_{ME} has larger magnitude in the historical period than E_{LM}, the change of globally integrated time-mean E under the greenhouse warming is primarily attributed to that of E_{ME}.

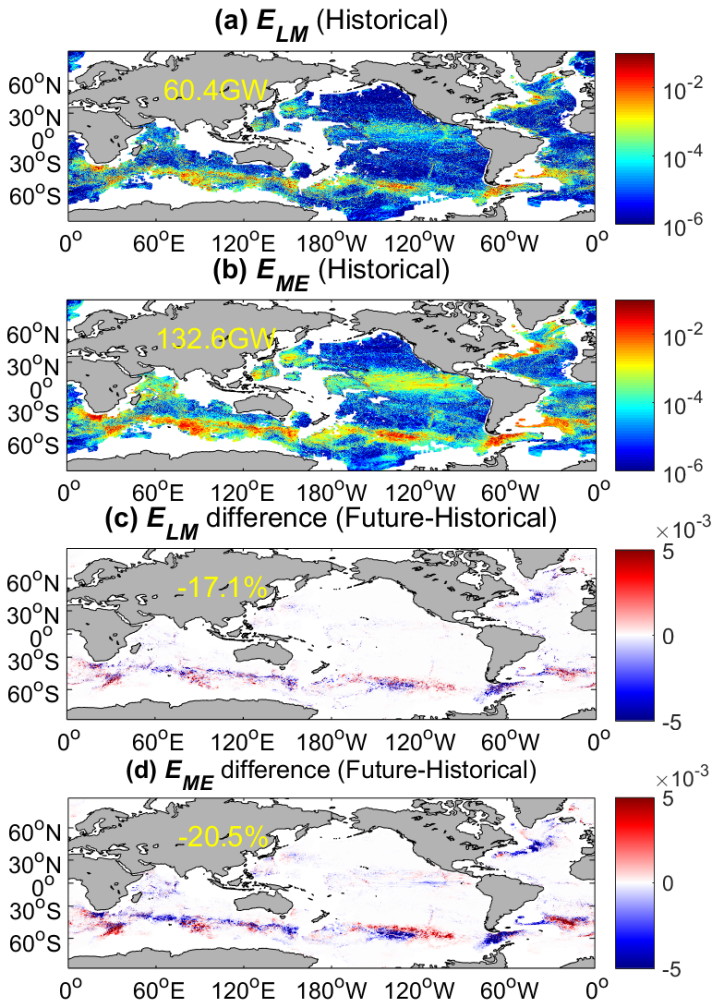

Figure 3. Time-mean energy conversion rate into lee waves contributed by (a) large-scale mean flows E_{LM} and (b) mesoscale eddies E_{ME} (W/m^2) during 1930-1934 simulated by the CESM-HR. Regions where the topographic spectrum of G2010 is unavailable are masked by white. (c) and (d) Same as (a) and (b) but for the change of time-mean E_{LM} and E_{ME} during 2086-2090 relative to their counterparts during 1930-1934. Yellow numbers indicate the globally integrated time-mean E_{LM} and E_{ME} in (a, b) and their percentage changes under the greenhouse warming in (c, d).

4 Discussion

One tuning parameter in the computation of Eq. (1) is Fr_c that accounts for the saturation of E over the super-critical topography (Nikurashin & Ferrari, 2010). Although Fr_c is set as 0.5 in this study, it is worth pointing out that other values like 0.4 and 0.75 are also adopted in the existing literature (Nikurashin et al., 2014; Scott et al., 2011). To evaluate to what extent the uncertainties in Fr_c affect the change of E under the greenhouse warming, we perform sensitivity tests by varying the value of Fr_c from 0.4 to 0.75. The globally integrated time-mean E during

1930-1934 increases sublinearly with the increasing Fr_c, ranging from 179.4±2.8 GW for Fr_c = 0.4 to 218.3±3.4 GW for Fr_c = 0.75 (Table 1). This sublinear dependence of the globally integrated time-mean E on Fr_c is because a large fraction of E is contributed from the SO where Fr is generally less than 0.4 (Figure. 4) so that the value of E does not change for Fr_c varying from 0.4 to 0.75. Although Fr_c has some noticeable influences on the globally integrated time-mean E, the reduction of the globally integrated time-mean E is robust regardless of the value of Fr_c. The globally integrated time-mean E during 2086-2090 decreases by 20.6%, 19.4% and 22.4% compared to their counterparts during 1930-1934 for Fr_c = 0.4, 0.5 and 0.75, respectively. We conclude that the uncertainties in Fr_c does not have a substantial impact on the percentage change of E under the greenhouse warming.

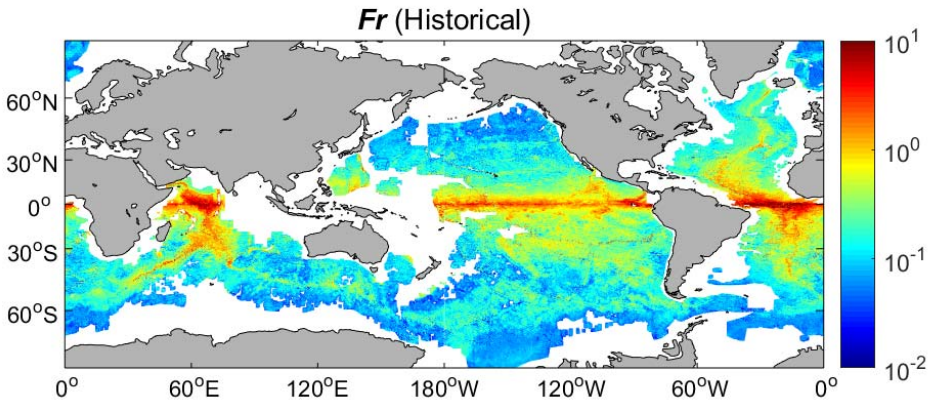

Figure 4. Time-mean Froude number Fr during 1930-1934 simulated by the CESM-HR.

5 Summary

In this study, we investigated the response of energy conversion into lee waves to the greenhouse warming by applying the linear theory of lee wave generation to the climate simulation of the CESM-HR resolving mesoscale eddies. The globally integrated time-mean E during the historical period (1930-1934) is estimated to be 193.0±3.0 GW, with the lee wave generation over the SO making dominant contribution. Under the high carbon emission scenario, the globally integrated time-mean E during 2086-2090 decreases by ~20% compared to that during 1930-1934. This decrease is attributed to the weakened bottom large-scale mean flows, mesoscale eddies and stratification under the greenhouse warming.

Our findings are qualitatively consistent with those reported by Melet et al. (2015). However, the projected reduction of E by the CESM-HR is quantitatively more evident than that (a 20% decrease by the end of the 22nd century) projected by the coarse-resolution CGCM used by Melet et al. (2015). This difference may result from two aspects. First, although Melet et al. (2015) found that the change of N_b has little effect on the change of E under the greenhouse warming, N_b is projected by the CESM-HR to be reduced (Figure. 2a) and contributes importantly to the reduced E (Table 1). We note that the projected reduction of N_b by the

CESM-HR is consistent with the projections by the high-resolution CMIP6 CGCMs (Figure S2), lending support to its reliability. Second, the weakened mesoscale eddy flows near the sea floor projected by the CESM-HR make important contribution to the reduction of E under the greenhouse warming, whereas such effects are absent in the coarse-resolution CGCM of Melet et al. (2015), suggesting the deficiencies of mesoscale eddy parameterization used by Melet et al. (2015).

The globally integrated time-mean wind power on the surface geostrophic flows remains nearly unchanged between 1930-1934 (0.69±0.01 TW) and 2086-2090 (0.75±0.01 TW). The significant reduction of E under the greenhouse warming thus suggests that the lee wave generation becomes less efficient in dissipating the wind-driven ocean circulations. Furthermore, the reduced E implies weakened energy source of turbulent diapycnal mixing. Changes of these processes have not been parameterized in the current generation of CGCMs but are likely to play an important role in regulating the ocean's heat uptake and carbon sequestration under the greenhouse warming.

Finally, this study does not take into account the impact of the greenhouse warming on the lee wave-geostrophic flow interactions during the upward radiation of lee waves. Recent studies (e.g., Baker & Mashayek et al., 2021; Kunze & Lien, 2019; Sun et al., 2022; Wu et al., 2022; Yang et al., 2023a) suggest that lee wave-geostrophic flow interactions can either transfer energy from lee waves to geostrophic flows or the opposite. The greenhouse warming does not only affect N_b and $\mathbf{U}_b$ but also the vertical structure of geostrophic flows in the ocean interior (Peng et al., 2022), with the later playing a key role in the energy exchange between geostrophic flows and lee waves (Kunze & Lien, 2019). The impact of the greenhouse warming on the lee wave-geostrophic flow interactions is left for a future study.

Acknowledgments

This work is supported by Marine S&T Fund of Shandong Province for Laoshan Laboratory (2022QNLM010302) and Taishan Scholar Funds (tsqn201909052). We thank John Goff for providing the abyssal hill topography products and Laoshan Laboratory for the support of computing resources.

Open Research

The CESM-HR output can be downloaded from the website https://ihesp.github.io/archive/products/ds_archive/Sunway_Runs.html by selecting the tab "500-YEAR 1850 PRE-INDUSTRIAL CONTROL" and "250-YEAR 1850 TRANSIENT SIMULATIONS". The CMIP6 model data can be downloaded from https://esgf-node.llnl.gov/search/cmip6/. The CMIP6 CGCMs used in this study are listed in Table S1 in the Supporting Information.

References

Aguilar, D. A., & Sutherland, B. R. (2006). Internal wave generation from rough topography. Physics of Fluids, 18(6). https://doi.org/10.1063/1.2214538.

Baker, L. E., & Mashayek, A. (2021). Surface reflection of bottom generated oceanic lee waves. Journal of Fluid Mechanics, 924(Bell 1975), 1–34. https://doi.org/10.1017/jfm.2021.627.

Baker, L. E., & Mashayek, A. (2022). The impact of realistic topographic representation of the parameterisation of lee wave energy flux. Journal of Geophysical Research: Oceans, 127(10), e2022JC018995. https://doi.org/10.1029/2022JC018995.

Beech, N., Rackow, T., Semmler, T., Danilov, S., Wang, Q., & Jung, T. (2022). Long-term evolution of ocean eddy activity in a warming world. Nature Climate Change, 12(10), 910–917. https://doi.org/10.1038/s41558-022-01478-3.

Bell, T. H. (1975a). Lee waves in stratified flows with simple harmonic time dependence. Journal of Fluid Mechanics, 67(4), 705–722. https://doi.org/10.1017/s0022112075000560.

Bell, T. H. (1975b). Topographically generated internal waves in the open ocean. Journal of Geophysical Research, 80(3), 320–327. https://doi.org/10.1029/JC080i003p00320.

Brearley, J. A., Sheen, K. L., Garabato, A. C. N., Smeed, D. A., & Waterman, S. (2013). Eddy-induced modulation of turbulent dissipation over rough topography in the Southern Ocean. Journal of Physical Oceanography, 43, 2288–2308. https://doi.org/10.1175/jpo-d-12-0222.1.

Chang, P., Zhang, S., Danabasoglu, G., Yeager, S. G., Fu, H., Wang, H., et al. (2020). An unprecedented set of high-resolution Earth system simulations for understanding multiscale interactions in climate variability and change. Journal of Advances in Modeling Earth Systems, 12(12), e2020MS002298. https://doi.org/10.1029/2020MS002298.

373 Chen, C., Wang, G., Xie, S. P., & Liu, W. (2019). Why does global warming weaken the Gulf
374 Stream but intensify the Kuroshio? Journal of Climate, 32(21), 7437–7451.
375 https://doi.org/10.1175/JCLI-D-18-0895.1.
376 Clément, L., Frajka-Williams, E., Sheen, K. L., Brearley, J. A., & Naveira Garabato, A. C.
377 (2016). Generation of internal waves by eddies impinging on the western boundary of the North
378 Atlantic. Journal of Physical Oceanography, 46(4), 1067–1079. https://doi.org/10.1175/JPO-D-
379 14-0241.1.
380 Cusack, J. M., Naveira Garabato, A. C., Smeed, D. A., & Girton, J. B. (2017). Observation of a
381 large Lee wave in the Drake Passage. Journal of Physical Oceanography, 47(4), 793–810.
382 https://doi.org/10.1175/JPO-D-16-0153.1.
383 Eden, C., & Greatbatch, R. J. (2008). Towards a mesoscale eddy closure. Ocean Modelling,
384 20(3), 223–239. https://doi.org/10.1016/j.ocemod.2007.09.002.
385 Evans, D. G., Frajka-Williams, E., Naveira Garabato, A. C., Polzin, K. L., & Forryan, A. (2020).
386 Mesoscale Eddy Dissipation by a “Zoo” of Submesoscale Processes at a Western Boundary.
387 Journal of Geophysical Research: Oceans, 125(11), 1–25.
388 https://doi.org/10.1029/2020JC016246.
389 Eyring, V., Bony, S., Meehl, G. A., Senior, C. A., Stevens, B., Stouffer, R. J., & Taylor, K. E.
390 (2016). Overview of the coupled model intercomparison project phase 6 (CMIP6) experimental
391 design and organization. Geoscientific Model Development, 9(5), 1937–1958.
392 https://doi.org/10.5194/gmd-9-1937-2016.
393 Ferrari, R., & Wunsch, C. (2009). Ocean circulation kinetic energy: Reservoirs, sources, and
394 sinks. Annual Review of Fluid Mechanics, 41, 253–282.
395 https://doi.org/10.1146/annurev.fluid.40.111406.102139.

Goff, J. A. (2010). Global prediction of abyssal hill root-mean-square heights from small-scale altimetric gravity variability. Journal of Geophysical Research: Solid Earth, 115(12), 1–16. https://doi.org/10.1029/2010JB007867.

Goff, J. A., & Jordan, T. H. (1988). Stochastic modeling of seafloor morphology: Inversion of sea beam data for second-order statistics. Journal of Geophysical Research, 93(B11), 13589–13608. https://doi.org/10.1029/JB093iB11p13589.

Hu, Q., Huang, X., Zhang, Z., Zhang, X., Xu, X., Sun, H., et al. (2020). Cascade of internal wave energy catalyzed by eddy-topography interactions in the deep South China Sea. Geophysical Research Letters, 47(4), 1–10. https://doi.org/10.1029/2019GL086510.

Kunze, E., & Lien, R. C. (2019). Energy sinks for lee waves in shear flow. Journal of Physical Oceanography, 49(11), 2851–2865. https://doi.org/10.1175/JPO-D-19-0052.1.

Munk, W., & Wunsch, C. (1998). Abyssal recipes II: Energetics of tidal and wind mixing. Deep Sea Research Part I: Oceanographic Research Papers, 45(12), 1977–2010. https://doi.org/10.1016/s0967-0637(98)00070-3.

Marshall, D. P., & Adcroft, A. J. (2010). Parameterization of ocean eddies: Potential vorticity mixing, energetics and Arnold's first stability theorem. *Ocean Modelling*, 32(3–4), 188–204. https://doi.org/10.1016/j.ocemod.2010.02.001.

Melet, A., Hallberg, R., Adcroft, A., Nikurashin, M., & Legg, S. (2015). Energy flux into internal lee waves: Sensitivity to future climate changes using linear theory and a climate model. *Journal of Climate*, 28(6), 2365–2384. https://doi.org/10.1175/JCLI-D-14-00432.1.

Melet, A., Hallberg, R., Legg, S., & Nikurashin, M. (2014). Sensitivity of the ocean state to lee wave-driven mixing. *Journal of Physical Oceanography*, 44(3), 900–921. https://doi.org/10.1175/JPO-D-13-072.1.

Meyer, A., Polzin, K. L., Sloyan, B. M., & Phillips, H. E. (2016). Internal waves and mixing near the Kerguelen Plateau. *Journal of Physical Oceanography*, 46(2), 417–437. https://doi.org/10.1175/JPO-D-15-0055.1.

Nikurashin, M., & Ferrari, R. (2010). Radiation and dissipation of internal waves generated by geostrophic motions impinging on small-scale topography: Theory. *Journal of Physical Oceanography*, 40(5), 1055–1074. https://doi.org/10.1175/2009JPO4199.1.

Nikurashin, M., & Ferrari, R. (2011). Global energy conversion rate from geostrophic flows into internal lee waves in the deep ocean. *Geophysical Research Letters*, 38(8), 1–6. https://doi.org/10.1029/2011GL046576.

Nikurashin, M., Ferrari, R., Grisouard, N., & Polzin, K. (2014). The impact of finite-amplitude bottom topography on internal wave generation in the Southern Ocean. Journal of Physical Oceanography, 44(11), 2938‑2950. https://doi.org/10.1175/JPO-D-13-0201.1

Nikurashin, M., Vallis, G. K., & Adcroft, A. (2013). Routes to energy dissipation for geostrophic flows in the Southern Ocean. *Nature Geoscience*, 6(1), 48–51. https://doi.org/10.1038/ngeo1657.

Scott, R. B., Goff, J. A., Naveira Garabato, A. C., & Nurser, A. J. G. (2011). Global rate and spectral characteristics of internal gravity wave generation by geostrophic flow over topography. *Journal of Geophysical Research: Oceans*, 116(9), 1–14. https://doi.org/10.1029/2011JC007005.

Sun, H., Yang, Q., Zheng, K., Zhao, W., Huang, X., & Tian, J. (2022). Internal lee waves generated by shear flow over small-scale topography. *Journal of Geophysical Research: Oceans*, 127(6), 1–28. https://doi.org/10.1029/2022JC018547.

Trossman, D. S., Arbic, B. K., Garner, S. T., Goff, J. A., Jayne, S. R., Metzger, E. J., & Wallcraft, A. J. (2013). Impact of parameterized lee wave drag on the energy budget of an

441 eddying global ocean model. *Ocean Modelling*, 72, 119–142.
442 https://doi.org/10.1016/j.ocemod.2013.08.006.
443 Trossman, D. S., Arbic, B. K., Richman, J. G., Garner, S. T., Jayne, S. R., & Wallcraft, A. J.
444 (2016). Impact of topographic internal lee wave drag on an eddying global ocean model. *Ocean*
445 *Modelling*, 97, 109–128. https://doi.org/10.1016/j.ocemod.2015.10.013.
446 Peng, Q., Xie, S. P., Wang, D., Huang, R. X., Chen, G., Shu, Y., et al. (2022). Surface warming–
447 induced global acceleration of upper ocean currents. *Science Advances*, 8(16).
448 https://doi.org/10.1126/sciadv.abj8394.
449 Wright, C. J., Scott, R. B., Ailliot, P., & Furnival, D. (2014). Lee wave generation rates in the
450 deep ocean. *Geophysical Research Letters*, 41(7), 2434–2440.
451 https://doi.org/10.1002/2013GL059087.
452 Wu, Y., Kunze, E., Tandon, A., & Mahadevan, A. (2022). Reabsorption of lee-wave energy in
453 bottom-intensified currents. *Journal of Physical Oceanography*. https://doi.org/10.1175/jpo-d-
454 22-0058.1.
455 Wunsch, C. (1999). The work done by the wind on the oceanic general circulation. *Journal of*
456 *Physical Oceanography*, 28(11), 2332–2342. https://doi.org/10.1175/1520-
457 0485(1998)028<2332:twdbtw>2.0.co;2.
458 Wunsch, C., & Ferrari, R. (2004). Vertical mixing, energy, and the general circulation of the
459 oceans. *Annual Review of Fluid Mechanics*, 36(1), 281–314.
460 https://doi.org/10.1146/annurev.fluid.36.050802.122121.
461 Yang, H., Lohmann, G., Wei, W., Dima, M., Ionita, M., & Liu, J. (2016). Intensification and
462 poleward shift of subtropical Western boundary currents in a warming climate. *Journal of*
463 *Geophysical Research: Oceans*, 121(7), 4928–4945. https://doi.org/10.1002/2015JC011513.

Yang, L., Nikurashin, M., Hogg, A. M., & Sloyan, B. M. (2018). Energy loss from transient eddies due to lee wave generation in the Southern Ocean. *Journal of Physical Oceanography*, 48(12), 2867–2885. https://doi.org/10.1175/JPO-D-18-0077.1.

Yang, Z., Zhai, X., Marshall, D. P., & Wang, G. (2021). An idealized model study of eddy energetics in the western boundary "graveyard." *Journal of Physical Oceanography*, 51(4), 1265–1282. https://doi.org/10.1175/jpo-d-19-0301.1.

Yang, Z., Jing, Z., & Zhai, X. (2022). Effect of small-scale topography on eddy dissipation in the northern South China Sea. *Journal of Physical Oceanography*, 52(10), 2397–2416. https://doi.org/10.1175/JPO-D-21-0208.1.

Yang, Z., Jing, Z., & Zhai, X. (2023a). Energy sinks for lee waves in the northern South China Sea. *Journal of Geophysical Research: Oceans*, 128(1), 1–18. https://doi.org/10.1029/2022jc019060.

Yang, Z., Jing, Z., & Zhai, X. (2023b). The role of small-scale topography in modulating eddy scale in the northern South China Sea. *Journal of Geophysical Research: Oceans*, 128(3), 1–19. https://doi.org/10.1029/2022jc019524.

Table 1. The globally integrated time-mean energy conversion rate into lee waves E under different conditions of N_b and $\mathbf{U}_b$ and using different values of Fr_c. The errorbar corresponds to the 95% confidence interval.

N_b (s^{-1})	$\mathbf{U}_b$ (m/s)	Fr_c	E (GW)
Historical	Historical	0.5	193.0±3.0
Historical	Historical	0.4	179.4±2.8
Historical	Historical	0.75	218.3±3.4
Future	Future	0.5	155.5±4.8
Future	Future	0.4	142.4±4.2
Future	Future	0.75	169.3±5.6
Historical	Future	0.5	166.9±4.5
Future	Historical	0.5	176.5±3.2

Figure 1.

(a) N_b (Historical)

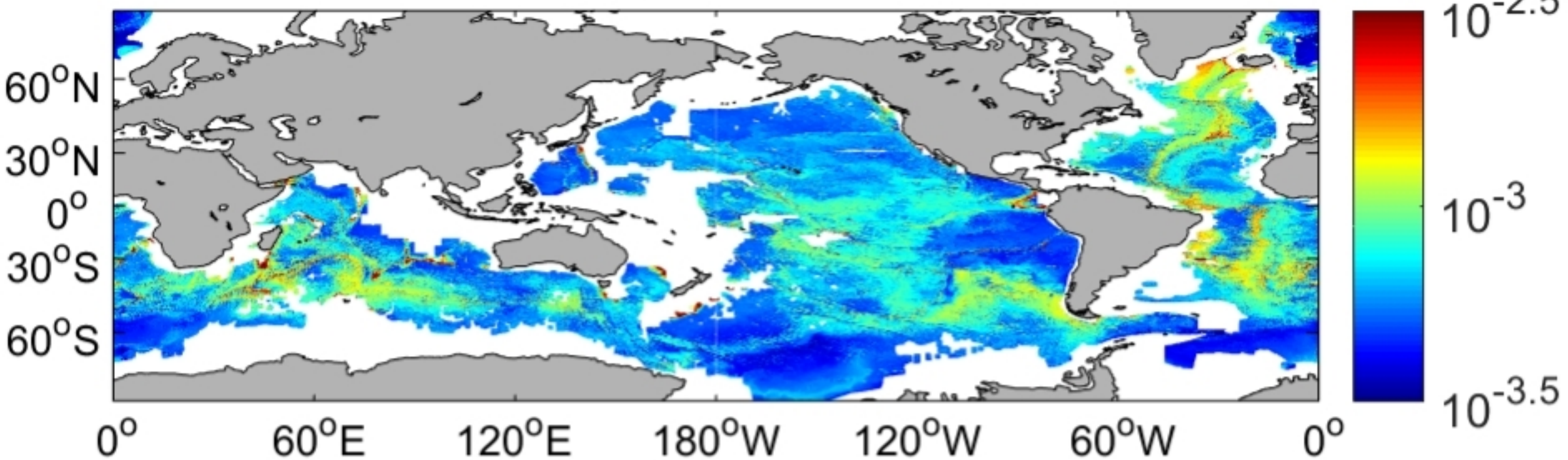

(b) KE_b (Historical)

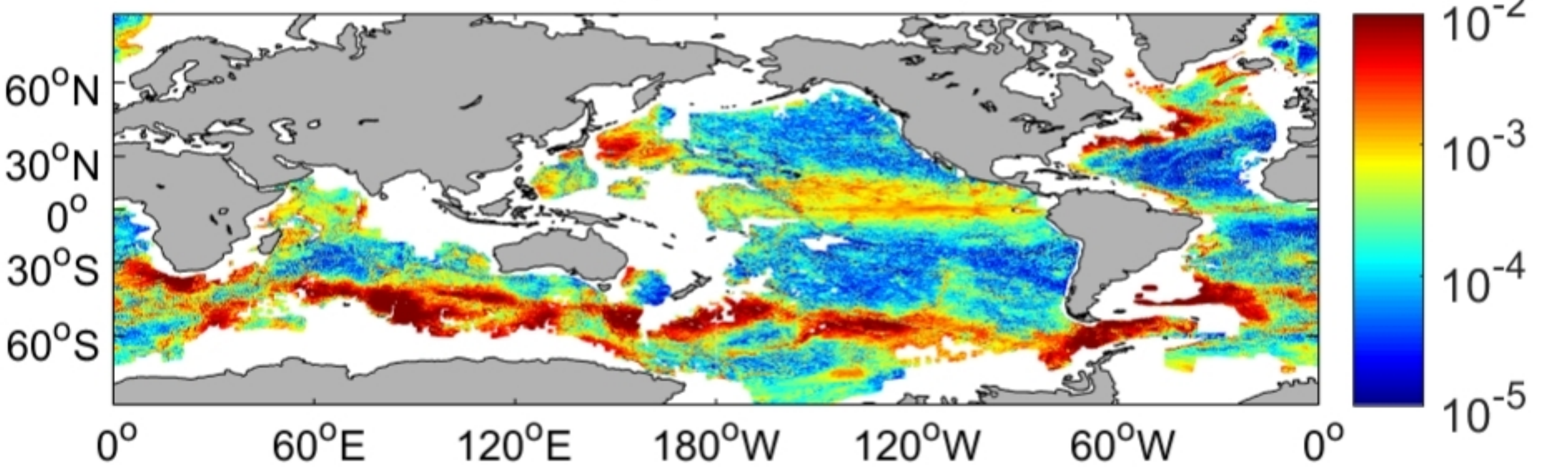

(c) E (Historical)

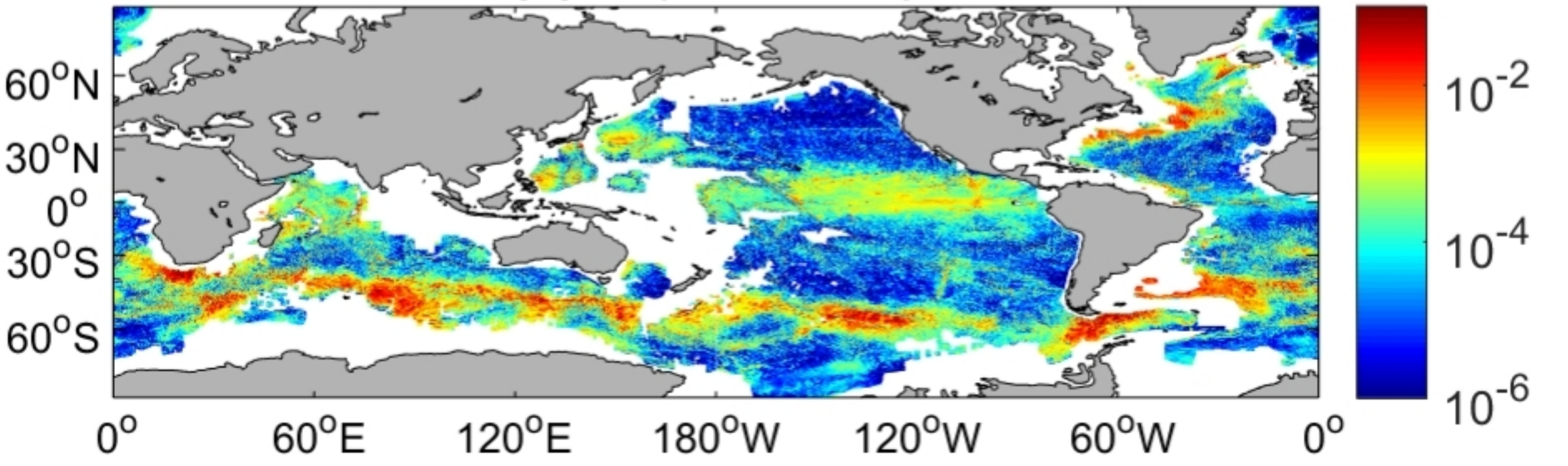

Figure 2.

(a) N_b difference (Future-Historical)

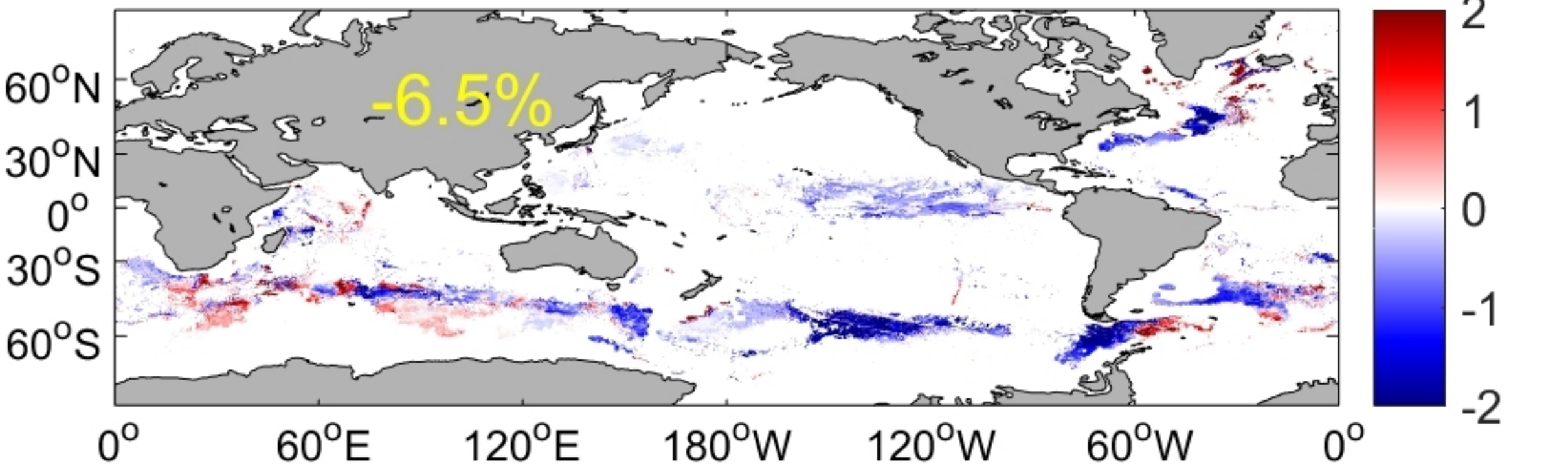

(b) KE_b difference (Future-Historical)

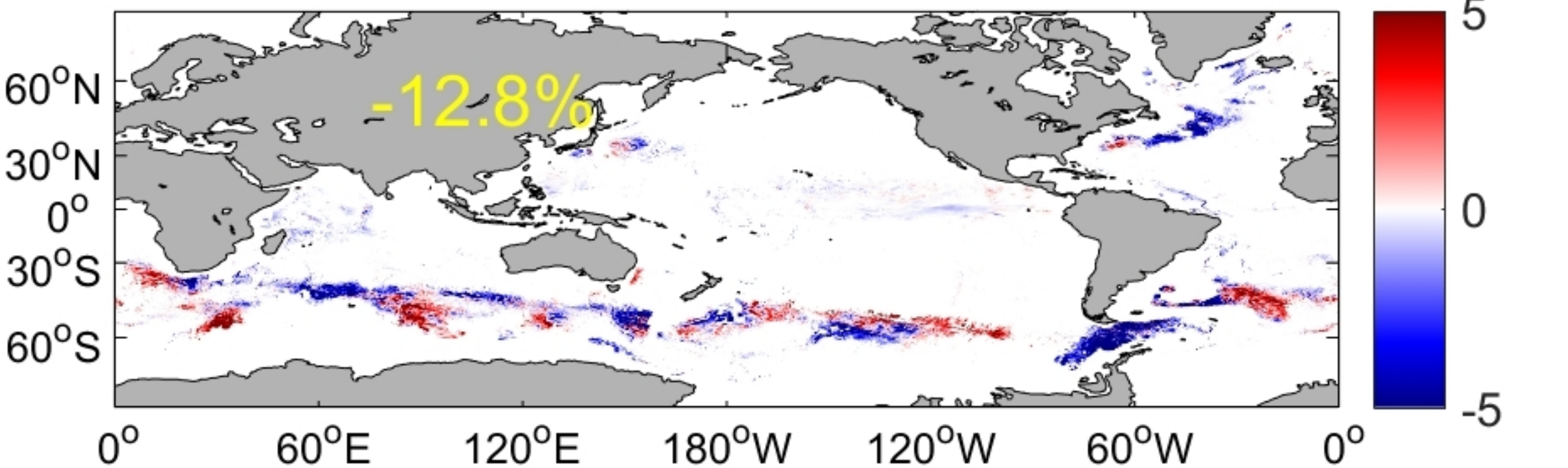

(c) E difference (Future-Historical)

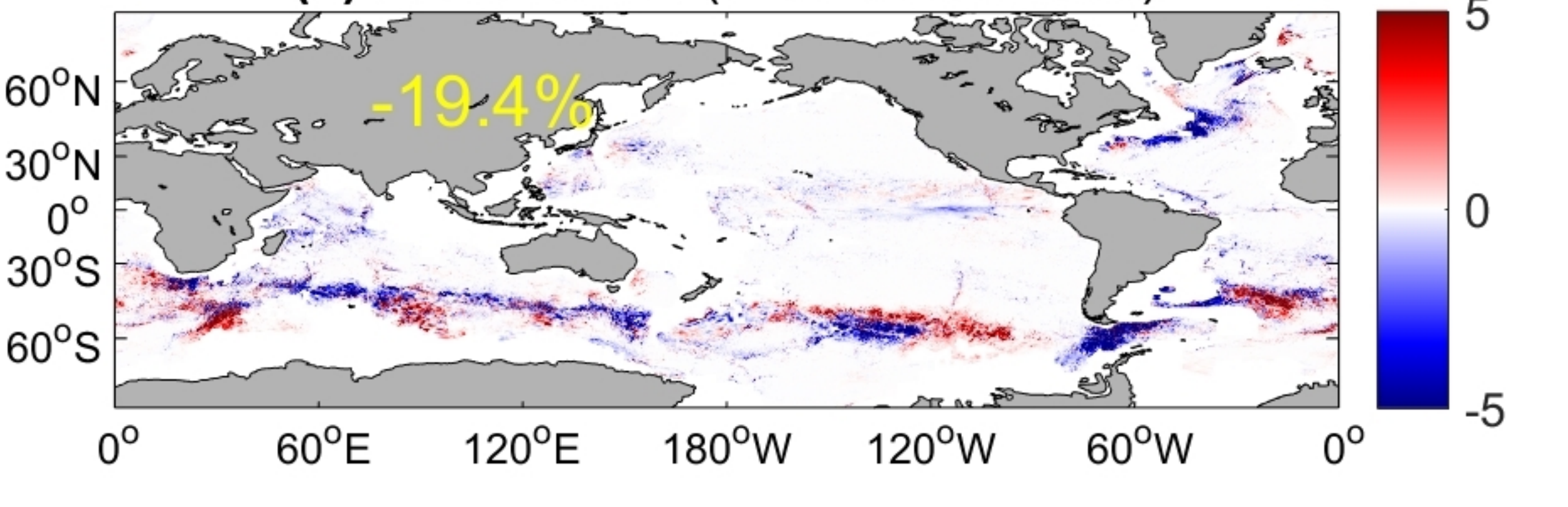

Figure 3.

(a) E_{LM} (Historical)

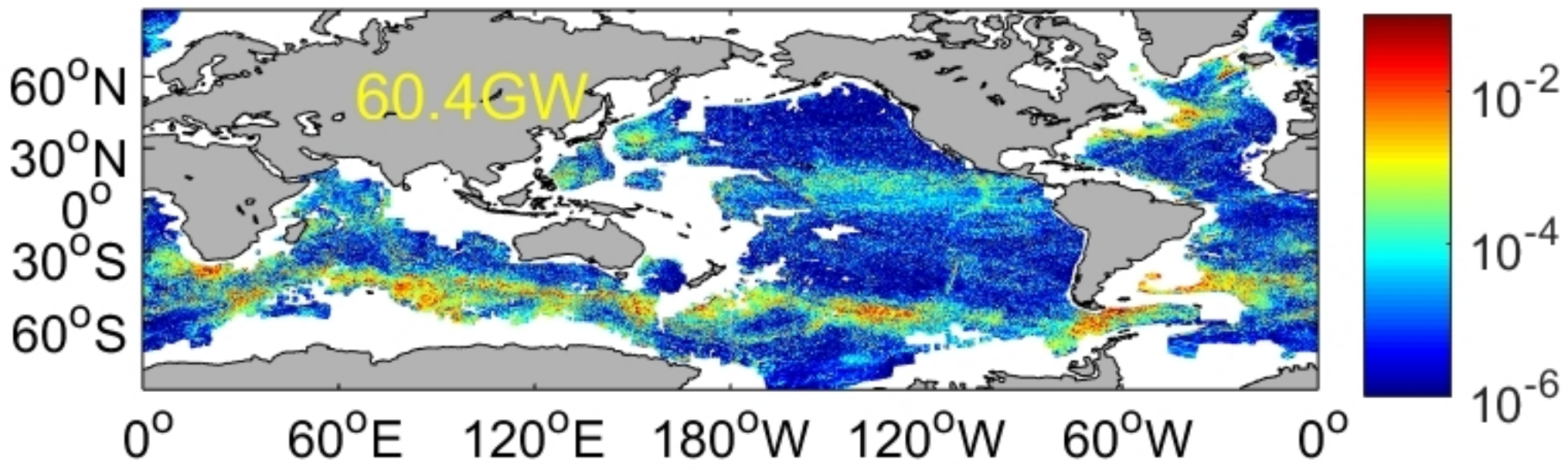

(b) E_{ME} (Historical)

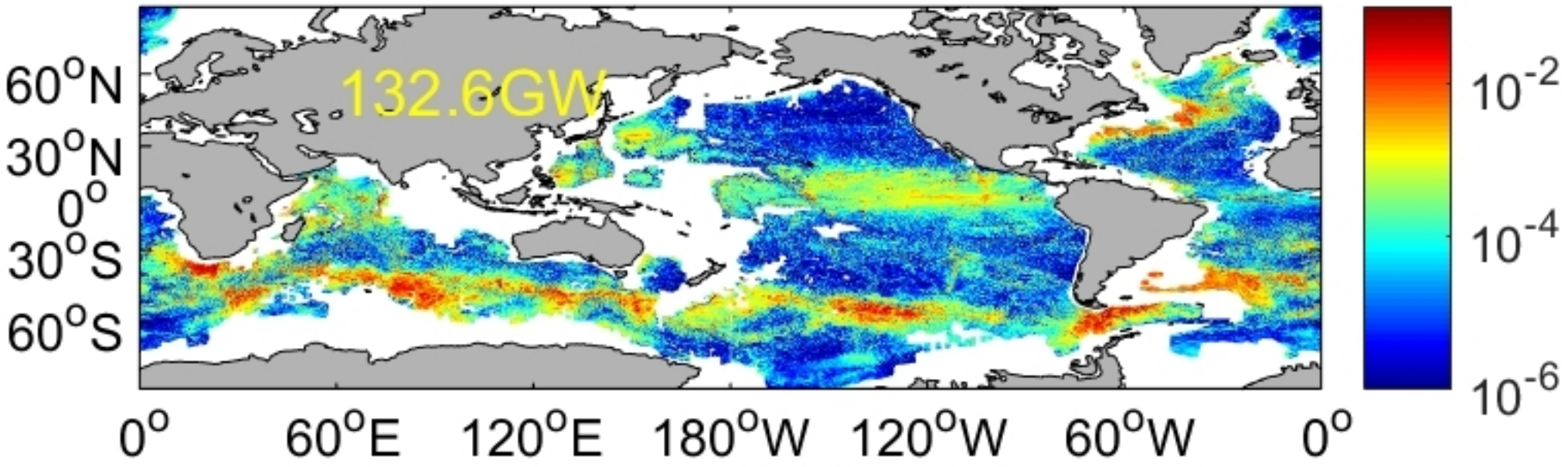

(c) E_{LM} difference (Future-Historical)

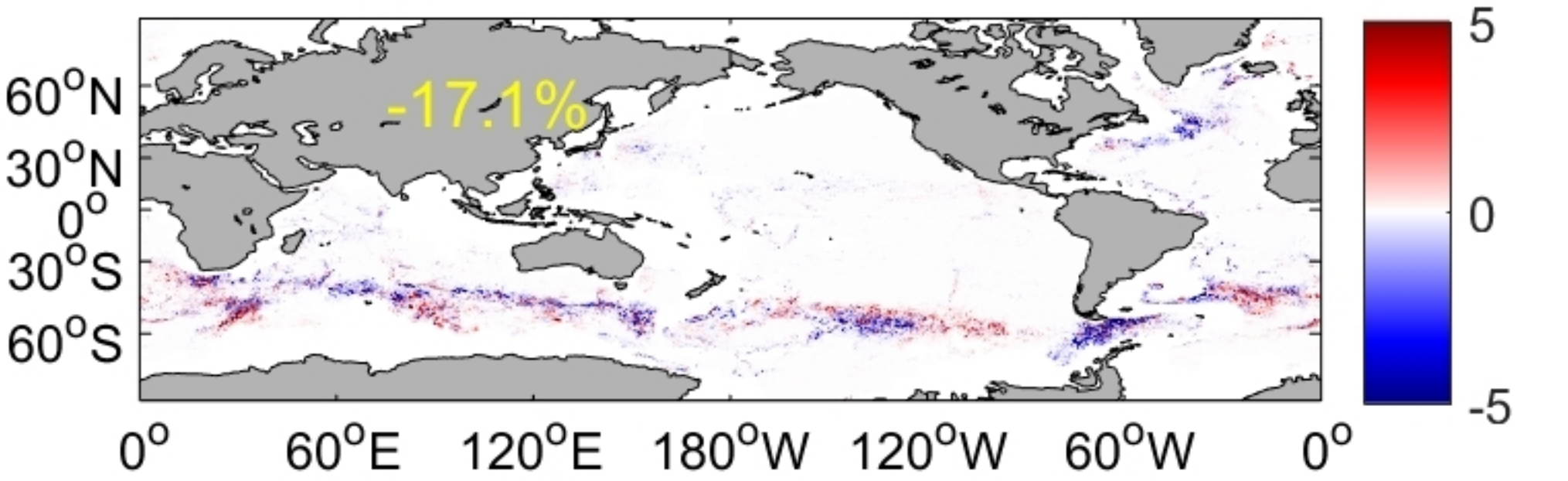

(d) E_{ME} difference (Future-Historical)

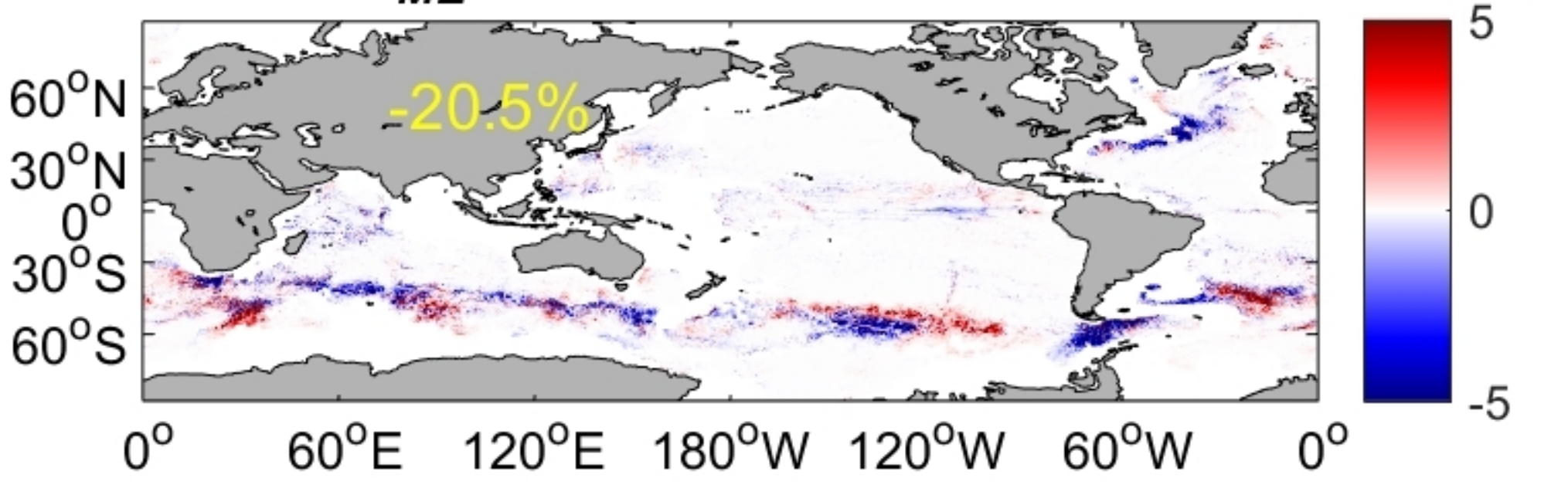

Figure 4.

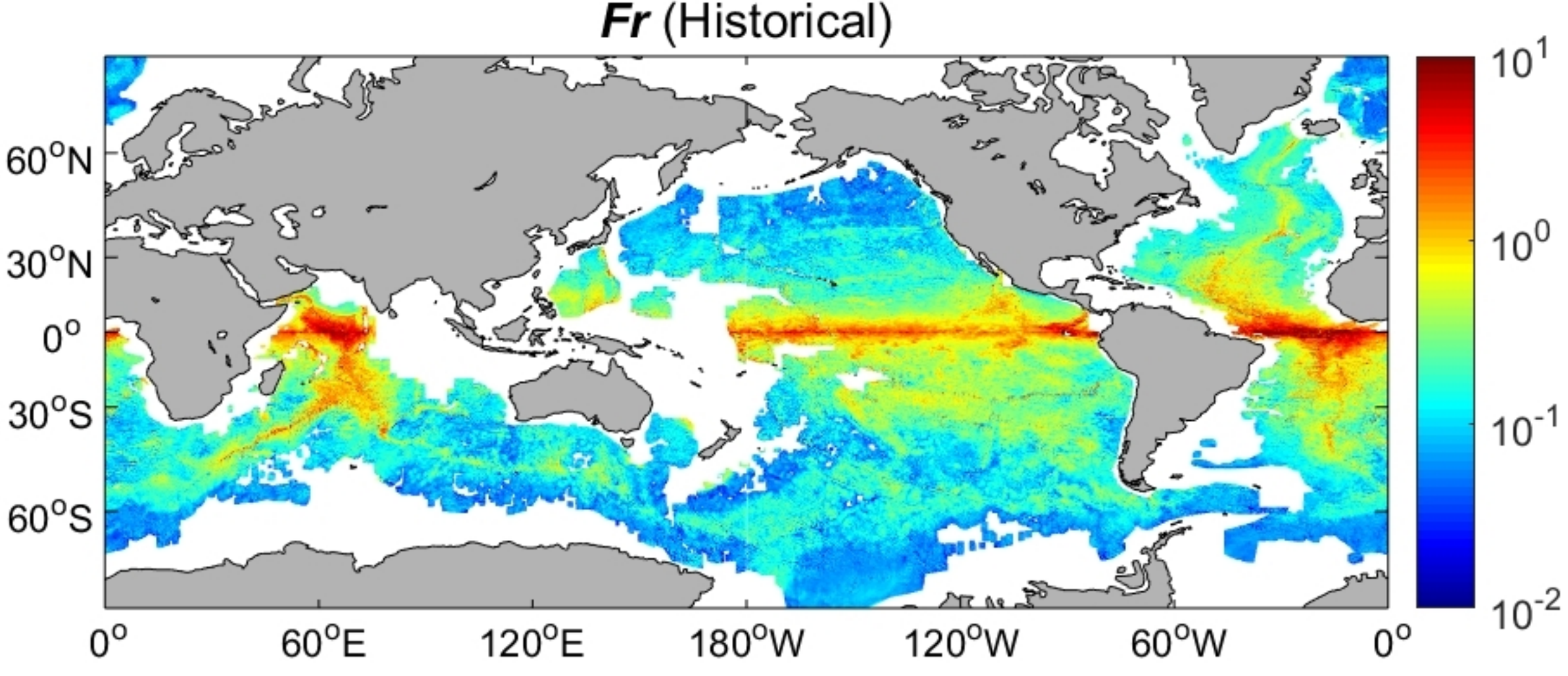
Fr (Historical)
60°N
30°N
0°
30°S
60°S
0°
60°E
120°E
180°W
120°W
60°W
0°
10^{1}
10^{0}
10^{-1}
10^{-2}